

Effects of Mesoscale Surface Thermal Heterogeneity on Low-Level Horizontal Wind Speeds

Song-Lak Kang · Donald Lenschow · Peter Sullivan

Received: 5 August 2011 / Accepted: 14 December 2011
© Springer Science+Business Media B.V. 2012

Abstract Using large-eddy simulation, we investigate characteristics of horizontal wind speed at 100 m above the ground, with surface heat-flux variations that are sinusoidal with amplitudes of 0, 50, and 200 W m^{-2} and wavelengths of 16, 32, and 128 km, and no background flow. When the amplitude is 200 W m^{-2} , wind speeds induced by the surface-flux variations on scales of 16 and/or 32 km have multiple temporal oscillations from 0600 to 1800 local standard time. The positive peaks first appear before noon. In contrast, for wind speeds induced by the 128-km surface heterogeneity, a single oscillation occurs in the late afternoon, which is much larger than those generated by the 16- and 32-km surface heterogeneity. In addition, at the oscillation onset the kurtosis of the velocity increment over a distance of 1 km significantly increases, which implies intermittency in the generation of 1-km scale eddies. The spatially intermittent energy cascade generated by surface heterogeneity scaled down to 1-km eddies is analogous to the well-known intermittent energy cascade in the inertial subrange. The kurtosis of the 1-km eddies is much larger with the 128-km surface heterogeneity than with the 16- and 32-km heterogeneities. Thus we conclude that localized rapid changes of low-level horizontal wind speed may be caused by significant local surface heterogeneity on scales between a few tens and a few hundreds of kilometres.

Keywords Diurnal evolution · Energy cascade · Horizontal wind · Large-eddy simulation · Surface-flux heterogeneity · Temporal oscillation · Velocity increment

1 Introduction

Differential solar heating at the earth's surface generates horizontal winds on various spatial scales. The sea breeze is a well-known example of a flow that is locally generated by

S.-L. Kang (✉)

Atmospheric Science Group, Department of Geosciences, Texas Tech University,
Box 42101, Lubbock, TX 79409-2101, USA
e-mail: song-lak.kang@ttu.edu

D. Lenschow · P. Sullivan
National Center for Atmospheric Research, Boulder, CO, USA

uneven surface heating. Similarly, adjacent inland areas that have contrasting surface properties, such as between irrigated/non-irrigated areas, bare/vegetated surfaces, and urban/rural regions, can generate sea-breeze-like local flows. Organized mesoscale winds are known by various names, including the “inland breeze” suggested by Mahrt et al. (1994). In order to improve the accuracy of wind forecasts, we need to more fully understand the characteristics of locally-generated mesoscale winds.

Although many characteristics of locally-generated mesoscale winds are known, many have not been adequately explored. For example, little attention has been paid to whether or not thermally-induced local winds are in a quasi-stationary state. Letzel and Raasch (2003) first suggested that thermally-induced mesoscale winds may trigger temporal oscillations in wind speed based on their large-eddy simulation (LES) experiments. Later, more LES-based studies (e.g., Esau 2007; Kang and Davis 2008; Wang 2009; Kang 2009) suggested that thermally-induced mesoscale winds may oscillate in time. Kang (2009) explained that when the amplitude of the surface heat-flux variation is high enough to level out the horizontal temperature gradient by horizontal advection, the generated mesoscale winds may undergo a transition from a quasi-stationary state to a non-stationary state, namely a temporally-oscillating mode.

Although numerous studies have investigated thermally-induced mesoscale winds, there have been few studies focusing on temporal oscillation and its associated abrupt wind-speed change. Analytical studies (e.g., Rotunno 1983; Dalu and Pielke 1993; Wang et al. 1996; Baldi et al. 2008) have used a linearized equation set that assumes a constant horizontal wind or have simply ignored advection terms. The linearized equation cannot explore the non-linear features of locally generated mesoscale winds such as temporal oscillations. Mesoscale models (MM), which are employed for many weather-related applications, can deal with non-linear processes. Many researchers have used mesoscale models to investigate characteristics of thermally-induced mesoscale winds as a function of scale and amplitude of the surface thermal forcing (e.g., Anthes 1984; Chen and Avissar 1994). However, the recent focus of mesoscale model-based studies has moved to sophisticated simulations with realistic surface and atmospheric conditions, and validation of the simulations with integrative measures such as precipitation (e.g., Holt et al. 2006; Zhang et al. 2009). In addition, mesoscale model-based studies have a major limitation in investigating detailed structures and processes in the atmospheric boundary layer (ABL), because the ABL is usually parameterized in a mesoscale model.

Most current ABL parametrizations used in mesoscale models do not consider the impact of locally-generated mesoscale flows on ABL structures and processes. A better understanding of locally-generated mesoscale flows and their influences on turbulence is likely to contribute to improved performance of numerical weather prediction (NWP) systems. For example, a better understanding of horizontal winds from the surface up to a few hundred metres may significantly increase the accuracy of wind-power forecasts (e.g., Giebel 2003; Rohrig and Lange 2007).

High spatial and temporal variability is an inherent property of low-level ABL flows (Lauren et al. 1999, 2001; Böttcher et al. 2003, 2007; Vindel et al. 2008; Muzy et al. 2010). Particularly in the inertial subrange the energy cascade from the energy injection scale down to the dissipation scale becomes increasingly intermittent with decreasing eddy size, which is contrary to Kolmogorov’s original hypothesis (Kolmogorov 1941) that the energy cascade is a self-similar, successive generation of space-filling eddies (Frisch 1995; Davidson 2004). The intermittency of wind speeds in the ABL has been studied by using probability density functions (PDFs) of observed velocity increments (e.g., Böttcher et al. 2003, 2007; Lauren et al. 2001). Previous studies of the intermittent turbulent energy cascade, however, have not

been related to the temporal oscillations of thermally-induced mesoscale winds, which are associated with an energy cascade process from the thermal forcing scale down to smaller scales (Kang 2009). We hypothesize that some of the spatially-discontinuous, temporally-abrupt changes in low-level horizontal wind speed are caused by local surface heterogeneity, particularly the surface thermal forcing on scales between a few tens and a few hundreds of kilometres.

Previous studies presenting temporal oscillations of thermally-induced horizontal flows used temporally invariant, single-scale surface heterogeneity (e.g., Letzel and Raasch 2003; Esau 2007; Kang and Davis 2008; Wang 2009; Kang 2009). Thus, the first goal of our study is to identify whether oscillations occur in thermally-induced horizontal winds under the following realistic conditions: (1) a diurnal cycle of surface heat-flux variation, (2) horizontal variations in surface heat flux at multiple scales, and (3) imposing the Coriolis force. In analyzing simulation results, however, we focus on the effects of the first two realistic conditions. Assuming that thermally-induced mesoscale flows still temporally oscillate under realistic conditions, the second goal is to investigate the wind-speed oscillations from the aspect of an analogy with the intermittent turbulent energy cascade in the inertial subrange.

Section 2 introduces the numerical experiments, while Sect. 3 provides results that focus on horizontal winds at 100 m above ground level. Section 4 summarizes and concludes the study.

2 Numerical Experiments

2.1 Model Description and Set-Up

We use the compressible and non-hydrostatic numerical model of Bryan and Fritsch (2002) to investigate ABL structures and processes over heterogeneous land surfaces (e.g., Kang and Davis 2008; Wang 2009; Kang 2009; Kang and Bryan 2011). The model integrates the filtered compressible Navier–Stokes equations using third-order Runge–Kutta time differencing and fifth-order spatial derivatives. This was found to be the most accurate finite-difference solution for simulating a highly non-linear flow by Wicker and Skamarock (2002). We use a fifth-order spatial derivative that has an inherent numerical dissipation, which makes the addition of explicit diffusion unnecessary (Bryan et al. 2003).

The model domain is 128 km in the x direction and 8 km in the y direction, with the horizontal grid spacing 100 m, and the vertical grid spacing 25 m. In both horizontal directions, the lateral boundary conditions are periodic. At the initial time, random perturbations of 0.1 K that initiate development of three-dimensional turbulence are superimposed on the potential temperature at the lowest atmospheric level. The upper boundary is a flat, rigid wall with a Rayleigh damping layer (Durran and Klemp 1983) occupying the first 1 km beneath the model top of 3.5 km, while the lower boundary is also a flat, rigid surface. The surface momentum flux is derived from a simple surface-drag parametrization (Stull 1988), and for a subfilter-scale (SFS) turbulence parametrization, we employ the turbulent kinetic energy scheme of Deardorff (1980). Due to the absence of appropriate observations, we used our numerical model to simulate the sheared convective boundary layer (CBL) over a uniform surface with the same experimental conditions used by Fedorovich et al. (2004). The results are insignificantly different from those of Fedorovich et al. (2004).

Vertical soundings of potential temperature and water vapour mixing ratio are obtained from the rawinsonde released at the Homestead site, USA (36.55°N, 100.6°W) at about 0750 local standard time (LST) on 25 May 2002 during the International H₂O Project (IHOP_2002;

Weckwerth et al. 2004). Following Findell and Eltahir (2003), the morning sounding has the convective triggering potential index (CTP) of 131 J kg^{-1} and a low-level humidity index (HI low) of 29 K , which is too dry for moist convection to develop. The dry sounding is purposely selected to exclude the effect of moist processes on the numerical experiments.

2.2 Surface Heat-Flux Variation

We prescribe the surface heat-flux variation in the x direction to be idealized sinusoids with amplitudes A_{F1} and A_{F2} , and wavelengths λ_{F1} and λ_{F2} ,

$$F_{\text{sfc}}(x) = \left(\langle F_{\text{sfc}} \rangle + A_{F1} \sin\left(\frac{2\pi}{\lambda_{F1}}x\right) + A_{F2} \sin\left(\frac{2\pi}{\lambda_{F2}}x\right) \right) \sin\left(\frac{2\pi}{T_0}t\right), \quad (1)$$

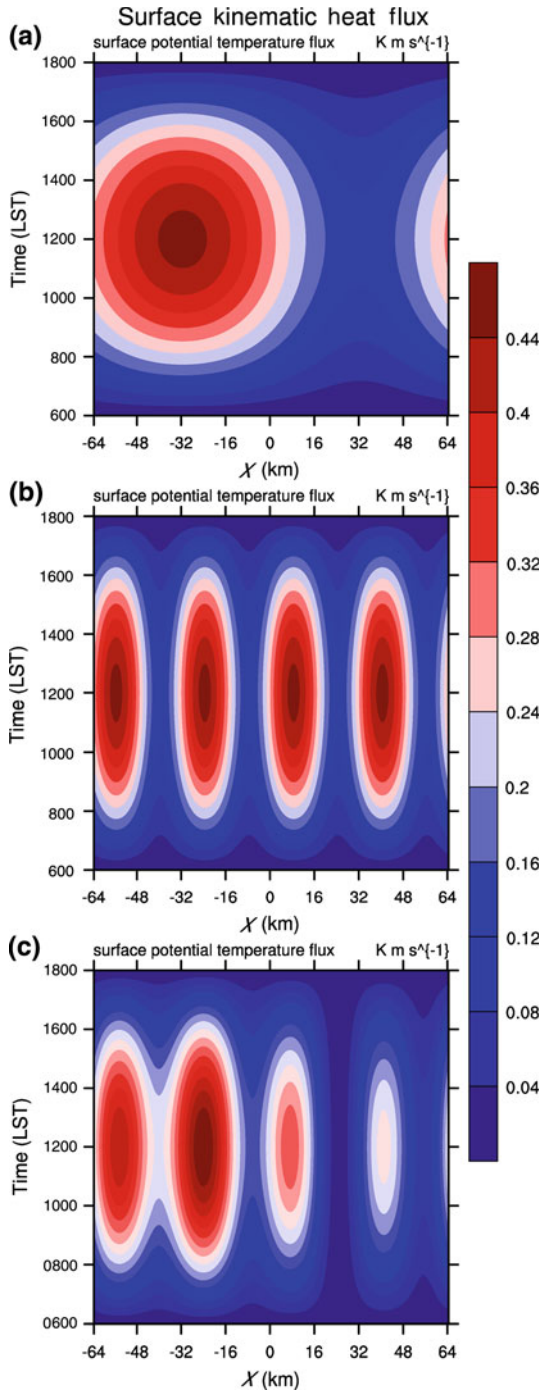
where $x = x' + 64 \text{ km}$ and x' ranges from -64 to 64 km . In (1), $\lambda_{F1} = 128 \text{ km}$ and $\lambda_{F2} = 32$ or 16 km . Equation 1 assumes that a smaller-scale surface heterogeneity is superimposed on larger-scale surface heterogeneity: here, obviously, the smaller scale is 32 or 16 km and the larger scale is 128 km . The amplitudes A_{F1} and A_{F2} are either $0, 0.0406 \text{ K m s}^{-1}$ (about 50 W m^{-2})¹ or $0.1625 \text{ K m s}^{-1}$ (about 200 W m^{-2}). The selection of the two amplitudes allows surface-heterogeneity-induced horizontal flows that are in quasi-stationary and non-stationary states. Surface heat-flux variations with an amplitude smaller than 100 W m^{-2} generate horizontal flows that are in a quasi-stationary state, while variations with an amplitude greater than 100 W m^{-2} generates non-stationary horizontal flows. In Eq. 1, $\langle F_{\text{sfc}} \rangle$ represents a domain average of the surface heat flux F_{sfc} . Here, $\langle F_{\text{sfc}} \rangle = 0.2924 \text{ K m s}^{-1}$ (about 360 W m^{-2}) or $0.3250 \text{ K m s}^{-1}$ (about 400 W m^{-2}), and T_0 is the length of day ($= 24 \text{ h}$). The domain-averaged heat flux $0.2924 \text{ K m s}^{-1}$ derives from an observed average over a 65-km aircraft track between 1103 and 1320 LST on $19 \text{ May } 2002$ during IHOP_2002 (for details, see Kang et al. 2007). The time t is in the range $0 \leq t \leq 12$, where $t = 0$ is sunrise (hereafter referred to as 0600 LST) and $t = 12$ is sunset (hereafter 1800 LST). The diurnal cycle of surface heat-flux variations is shown in Fig. 1. The amplitudes of the surface heat-flux variation have a minimum of zero at 0600 LST , then sinusoidally increase to a maximum value of 50 or 200 W m^{-2} at midday, and then sinusoidally decreasing to a minimum value of zero at 1800 LST . The amplitudes and wavelengths of the surface heat-flux variations used here are summarized in Table 1.

The amplitudes and wavelengths in Eq. 1 are used to label the numerical experiments. For example, A200L128 is the case with an amplitude of $0.1625 \text{ K m s}^{-1}$ (about 200 W m^{-2}) and a wavelength of 128 km . For the two-wavelength cases, the wavelength of 128 km is omitted in the nomenclature. For example, A050A200L016 is the case where the surface heat-flux variation of A200L016 is superimposed on that of A050L128. The cases with $A_{F1} = 0$ or $A_{F2} = 0$ in Eq. 1 are referred to as single-scale cases and those with $A_{F1} \neq 0$ and $A_{F2} \neq 0$ as multi-scale cases.

The two cases A200A200L032 and A200A200L016 have a maximum surface-flux difference of 800 W m^{-2} , obtained from smaller-scale (16-km scale or 32-km scale) surface-flux heterogeneity with a maximum difference of 400 W m^{-2} imposed on a 128-km scale surface heterogeneity that has a maximum difference of 400 W m^{-2} . This is large compared with IHOP_2002 observations. Kang and Davis (2008) estimated the mean and maximum values of the monotonically varying surface heat-flux difference between surface flux sites separated by about 20 km along an IHOP_2002 aircraft track between 1100 and 1400 LST for four

¹ Here, kinematic heat flux is converted to sensible heat flux by the product $\rho C_P = 1.231 \times 10^3 \text{ W m}^{-2} (\text{K m s}^{-1})^{-1}$ (Stull 1988), where ρ is air density and C_P is the specific heat of air at constant pressure.

Fig. 1 Surface kinematic heat flux prescribed in the numerical experiment for cases **a** A200L128, **b** A200L032, and **c** A200A200L032. The unit of the colour bar on the right is K m s^{-1}



days. They found a mean difference of 58 W m^{-2} and a maximum difference of 105 W m^{-2} . Although a difference of 800 W m^{-2} is somewhat extreme, many previous numerical studies have prescribed a surface-flux difference of $150\text{--}500 \text{ W m}^{-2}$ on various scales from a few

Table 1 Parameters characterizing the set of all cases

Case	$\langle F_{\text{sfc}} \rangle$ (K m s^{-1})	A_{F1} (K m s^{-1})	λ_{F1} (km)	A_{F2} (K m s^{-1})	λ_{F2} (km)
A000L000	0.2924	0	0	0	0
A200L128	0.2924	0.1625	128	0	0
A050L128	0.2924	0.0406	128	0	0
A200L032	0.2924	0	0	0.1625	32
A050L032	0.2924	0	0	0.0406	32
A200L016	0.2924	0	0	0.1625	16
A050L016	0.2924	0	0	0.0406	16
A200A200L032	0.3250	0.1625	128	0.1625	32
A200A200L016	0.3250	0.1625	128	0.1625	16
A200A050L032	0.2924	0.1625	128	0.0406	32
A200A050L016	0.2924	0.1625	128	0.0406	16
A050A200L032	0.2924	0.0406	128	0.1625	32
A050A200L016	0.2924	0.0406	128	0.1625	16
A050A050L032	0.2924	0.0406	128	0.0406	32
A050A050L016	0.2924	0.0406	128	0.0406	16

A_{F1} and A_{F2} represent the amplitudes of the surface heat-flux variation (1). λ_{F1} and λ_{F2} represents the wavelengths of the surface heat-flux variation. $\langle F_{\text{sfc}} \rangle$ represents a domain average of the surface heat-flux variation

kilometres to a few hundred kilometres (e.g., [Chen and Avissar 1994](#); [Shen and Leclerc 1995](#); [Avissar and Schmidt 1998](#); [Raasch and Harbusch 2001](#); [Weaver and Avissar 2001](#); [Letzel and Raasch 2003](#); [Hidalgo et al. 2010](#); [Liu et al. 2011](#)). In addition, there have now been observations of surface flux differences of $250\text{--}300 \text{ W m}^{-2}$ on scales smaller than a few hundred kilometre. For example, [Hidalgo et al. \(2008\)](#) observed afternoon surface sensible heat fluxes over the city of Toulouse, France that were 250 W m^{-2} higher than those over the nearby countryside. [Inoue et al. \(2005\)](#) observed the surface sensible heat flux over open water on scales of a few kilometres to be about 300 W m^{-2} , while the heat flux from the surrounding ice was about zero. [Courault et al. \(2005\)](#) observed surface heat-flux differences up to 250 W m^{-2} , with the highest values of 370 W m^{-2} for dry fields and the lowest of 120 W m^{-2} for the irrigated wheat. [Davis et al. \(2008\)](#) observed a surface heat-flux difference of 250 W m^{-2} on scales of a few kilometres within an urban area. Thus, considering that the surface-flux difference is smaller than 400 W m^{-2} on scales smaller than a few hundred kilometres, the prescribed surface heterogeneity is completely unrealistic. In addition, the purpose of this study is not to simulate real-case situations but to understand mechanisms and processes of temporally-oscillating mesoscale circulations induced by a high-amplitude surface heat-flux heterogeneity.

3 Results

3.1 Surface-Heterogeneity-Induced Horizontal Winds

Our simulations of daytime ABL flows induced by thermal surface heterogeneity over flat terrain with zero background flow focus on the horizontal wind component u , which is

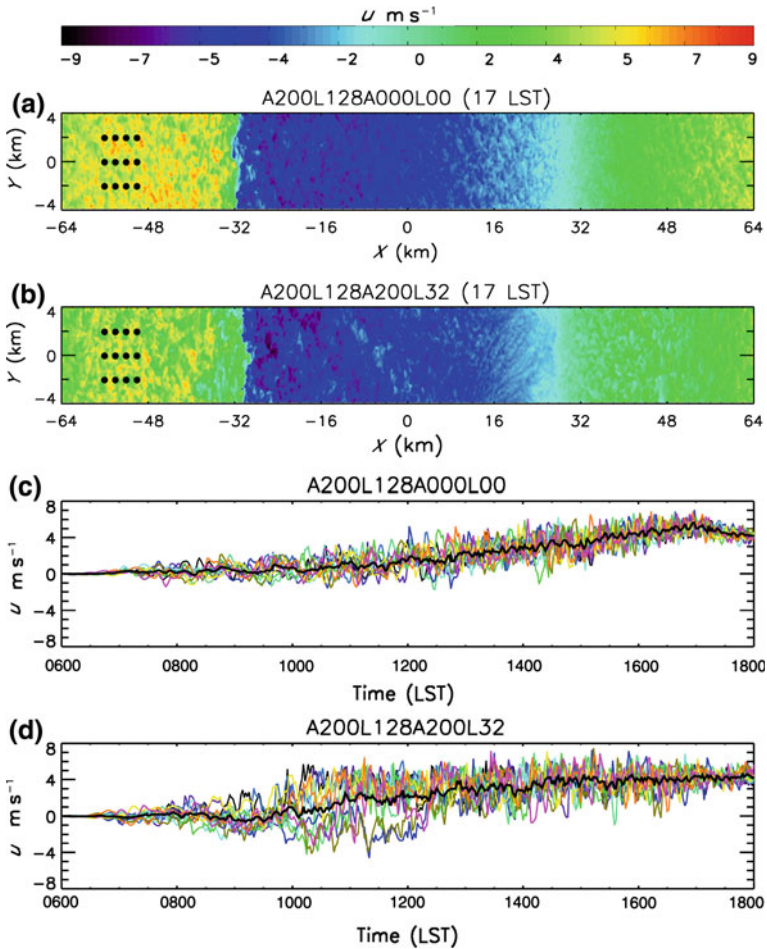
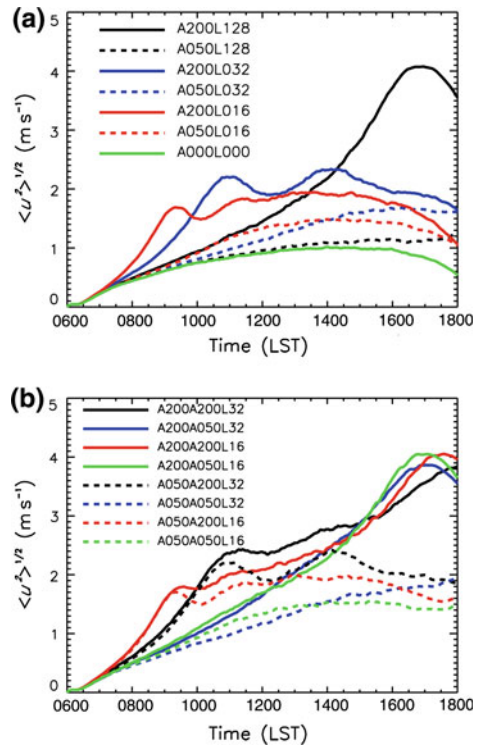


Fig. 2 Simulated u wind component, which is parallel to the direction of the prescribed surface heterogeneity, at 100-m height at 1700 LST for cases **a** A200L128 and **b** A200A200L032. For each case, the time series of u at the 12 specified locations marked with the symbols of filled circles in **(a)** and **(b)** are plotted in **c** for case A200L128 and **d** for case A200A200L032. The thick black line is a spatial average of u over the 12 sites

parallel to the direction of the surface heat-flux variation (1), at a height of 100 m above ground. Figure 2a, b present examples of u at 1700 LST, which are induced by the surface heterogeneity of A200L128 and A200A200L032, respectively. Also Fig. 2c, d present the time series of u at the 12 locations marked in Fig. 2a, b and the averages of u over the 12 locations. These examples demonstrate that characteristics of the induced horizontal flow can be significantly different depending on the surface heterogeneity, not only from the perspective of mesoscale fluctuations but also of the turbulence that is generated. Thus we study the surface-heterogeneity-induced horizontal flows from both perspectives.

First, we investigate characteristics of the induced horizontal flows from the perspective of the whole domain. Figure 3 shows the time evolution of the characteristic horizontal wind speed $\langle u^2 \rangle^{1/2}$, where $\langle \rangle$ denotes a domain average. It is obvious that the induced horizontal winds are temporally fluctuating when $A_{F1} = 200 \text{ W m}^{-2}$ or $A_{F2} = 200 \text{ W m}^{-2}$ in Eq. 1.

Fig. 3 **a** Time evolution of the characteristic wind speed $\langle u^2 \rangle^{1/2}$ for the single-scale cases, where $\langle \rangle$ denotes a domain average. **b** Time evolution of the characteristic wind speed $\langle u^2 \rangle^{1/2}$ for the multi-scale cases, where $\langle \rangle$ denotes a domain average



These results are consistent with previous studies (e.g., Letzel and Raasch 2003; Kang and Davis 2008; Kang 2009) that use temporally invariant, single-scale surface heterogeneity without the Coriolis force. However in this study we observe temporal oscillations in the low-level horizontal wind speeds that are induced by the diurnal cycle of surface heat flux, multiscale surface heterogeneity, and the Coriolis force.

In Fig. 3a, with smaller-scale surface heterogeneity, the oscillation onset of $\langle u^2 \rangle^{1/2}$ is earlier, but its oscillation amplitude is smaller. For case A200L016 (solid red line), which has the shortest surface heterogeneity wavelength of 16 km, the oscillation onset occurs at 0900 LST, which is two hours earlier than for case A200L032 (solid blue line), which has a wavelength of 32 km, and eight hours earlier than for case A200L128 (solid black line), which has the longest wavelength of 128 km. For case A200L032 (solid blue line) the second oscillation onset occurs at 1400 LST. The oscillation periodicity is about three hours. However, for case A200L016 (solid red line) the second oscillation onset is less obvious compared with that for case A200L032 (solid blue line), due to a smaller oscillation amplitude.

For case A200L128 (solid black line in Fig. 3a), the oscillation is much more obvious than in the smaller-scale surface variation cases (A200L016 and A200L032) due to its larger amplitude. However the temporal oscillation is not fully realized because its periodicity is longer than the daytime diurnal cycle of 12 h. In other words, for case A200L128, the second ramp of $\langle u^2 \rangle^{1/2}$ might occur if the surface were heated for much longer than a 24-h diurnal cycle. This result implies that it is unlikely that the horizontal flows induced by the surface heterogeneity on a scale somewhat larger than a few hundred kilometres are temporally fluctuating within a diurnal cycle. In other words, the horizontal flows induced by the

surface heterogeneity on a scale of several hundreds of kilometres or larger would be in a quasi-stationary mode.

Figure 3b presents the time evolutions of $\langle u^2 \rangle^{1/2}$ for the multi-scale surface variation cases. Basically the multi-scale case with A_{F1} and A_{F2} in Eq. 1 follows the single-scale case with A_{F2} ($\lambda_{F2} = 32$ or 16 km) earlier and then the single-scale case with A_{F1} ($\lambda_{F1} = 128$ km) later. For example, for all the multi-scale cases with $A_{F1} = 200 \text{ W m}^{-2}$ (solid lines in Fig. 3b), the oscillation onset occurs at 1700 LST in $\langle u^2 \rangle^{1/2}$, which is associated with the surface heterogeneity on a scale of $\lambda_{F1} = 128$ km. For the cases with $A_{F2} = 50 \text{ W m}^{-2}$ (A200A050L032: solid blue line, and A200A050L016: solid green line in Fig. 3b), $\langle u^2 \rangle^{1/2}$ steadily increases before the peak at 1700 LST. In contrast, for the cases with $A_{F2} = 200 \text{ W m}^{-2}$ (A200A200L032: solid black line, and A200A200L016: solid red line in Fig. 3b), $\langle u^2 \rangle^{1/2}$ experiences oscillation onsets between 0900 and 1400 LST, which are associated with the smaller-scale surface variations of 16 or 32 km. Thus it appears that the horizontal wind features induced by the two single-scale surface variations that make up the multi-scale surface variation remain in the horizontal winds induced by the multi-scale variation.

However, the time evolution of $\langle u^2 \rangle^{1/2}$ for a multi-scale case with A_{F1} and A_{F2} is not simply a linear combination of the two single-scale cases with A_{F1} and A_{F2} . For example in Fig. 3, the second peak of $\langle u^2 \rangle^{1/2}$ is obvious at 1400 LST for case A200L032 (solid blue line in Fig. 3a). For case A200A200L032 (solid black line in Fig. 3b), however, the second peak is inconspicuous, which is a result of non-linear interaction between large-scale and small-scale fluctuations.

3.2 Spectral Analysis

Using spectra we examine the oscillations of wind speed in terms of the energy cascade from surface heterogeneity mesoscales to smaller scales. The one-dimensional u spectrum $F_u(\kappa_1)$ is obtained by integrating the two-dimensional spectral density $\psi_u(\kappa_1, \kappa_2)$ along the κ_2 direction:

$$F_u(\kappa_1) = \int_{-\infty}^{\infty} \psi_u(\kappa_1, \kappa_2) d\kappa_2, \tag{2}$$

where κ_i ($i = 1, 2$) is defined as the wavenumber in the x_i direction. The x_1 (or x) direction is along the surface heterogeneity axis and the x_2 (or y) direction is orthogonal to the heterogeneity.

Figure 4 compares the u spectra from A200L032 (Fig. 4a) and A050L032 (Fig. 4b). For case A200L032, the spectra between 0900 and 1100 LST exhibit spectral density peaks at wavelengths smaller than the surface forcing scale of 32 km. In contrast, for case A050L032, $\langle u^2 \rangle^{1/2}$ steadily increases without any oscillation onset until the end of the daytime section of the diurnal cycle at 1800 LST (dashed blue line in Fig. 3a). In Fig. 4b, the spectra from A050L032 at the same period of 0900–1100 LST do not have a significant peak between the surface-variation scale of 32 km and the turbulence scale.

Similarly for case A200L128 (Fig. 5a), the absence of any clear spectral gap between the two spectral density peaks at the 128-km surface-heterogeneity scale and the turbulence scale indicates a cascade of spectral energy from the heterogeneity scale to smaller scales between 1600 and 1800 LST. However, for case A050L128 (Fig. 5b), a clear spectral gap between the surface-variation scale of 128 km and turbulence scale remains throughout the daytime diurnal cycle, which indicates no energy cascade from the 128-km heterogeneity scale to smaller scales.

Fig. 4 One-dimensional spectra of u at the height of 100 m at times of 0900, 1000, 1100 LST for cases **a** A200L032 and **b** A050L032. A short thick line corresponds to a $\kappa^{-5/3}$ spectrum

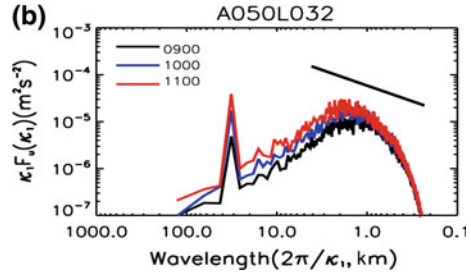
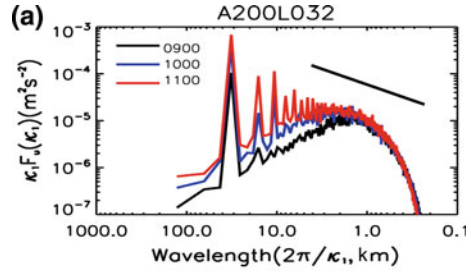
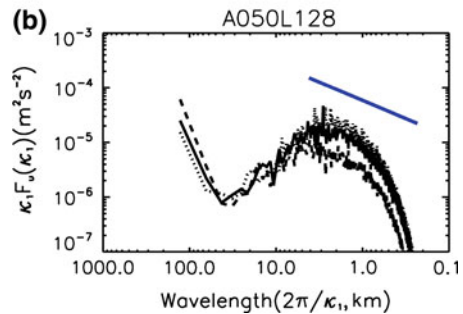
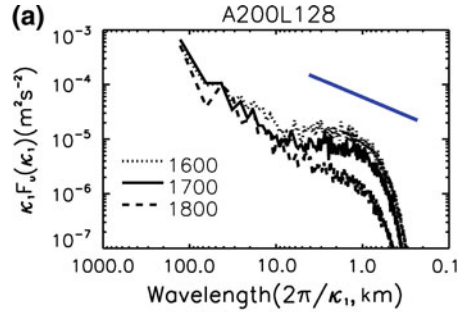


Fig. 5 One-dimensional spectra of u at the height of 100 m at times of 1600, 1700, 1800 LST for cases **a** A200L128 and **b** A050L128. A short thick line corresponds to a $\kappa^{-5/3}$ spectrum



For a multi-scale case, the energy cascade from the heterogeneity scales to smaller scales occurs at multiple times. For case A200A200L32 (solid black line in Fig. 3b), the time evolution of $\langle u^2 \rangle^{1/2}$ shows a peak at 1100 LST but a flattening at 1700 LST. Figure 6 shows u spectra at 1100 LST and 1700 LST from A200A200L32 (solid lines), and for comparison,

Fig. 6 One-dimensional spectra of u at the height of 100 m at times of **a** 1100 and **b** 1700 LST for cases A200A200L032, A200L128, and A200L032. A short thick line corresponds to a $\kappa^{-5/3}$ spectrum

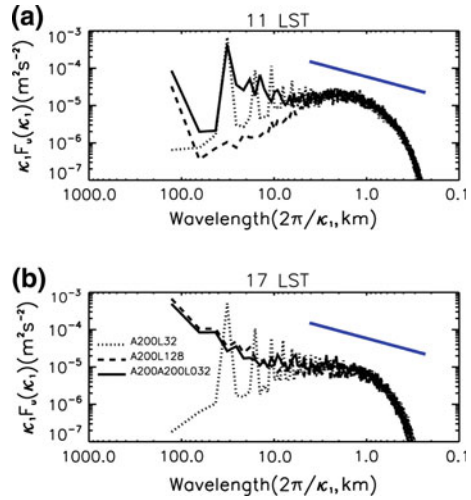


Fig. 6 also shows the spectra from the cases with two single-scale surface heterogeneities that make up the multi-scale surface heterogeneity of A200A200L032. For case A200L032 the wind-speed oscillation onset occurs at 1100 LST (solid blue line in Fig. 3a). At this time, there is no clear spectral gap between the surface-heterogeneity scale and turbulence scale (dotted line in Fig. 6a). However, for case A200L128 a spectral gap still exists (dashed line in Fig. 6a). The spectrum from the multi-scale case looks more like the spectrum from A200L032 rather than from A200L128 (solid line in Fig. 6a). However, at 1700 LST, the spectrum from case A200A200L032 follows the spectrum from A200L128 in which an oscillation onset occurs (Fig. 6b). In other words, the multi-scale case (A200A200L032) with $A_{F1} = A_{F2} = 200 \text{ W m}^{-2}$ in Eq. 1 initially follows A200L032 with $A_{F1} = 0$ and $A_{F2} = 200 \text{ W m}^{-2}$ and later A200L128 with $A_{F1} = 200 \text{ W m}^{-2}$ and $A_{F2} = 0$. After the oscillation onset at 1700 LST, however, if the multi-scale case A200A200L032 were to simply follow the single-scale case A200L128, $\langle u^2 \rangle^{1/2}$ should decrease, as shown in Fig. 3a (solid black line). The flattening of $\langle u^2 \rangle^{1/2}$ at 1700 LST (solid black line in Fig. 3b) is likely results from non-linear interactions between eddies cascading from the 128-km surface-heterogeneity scale and eddies associated with the 32-km surface-heterogeneity scale.

3.3 Scale Decomposition in Wavenumber Space

In the previous section, we identified energy cascades in the $\langle u^2 \rangle^{1/2}$ spectra. Here, we decompose u into different scale components by using a wave cut-off filter to investigate the energy cascade processes. This filter has been used for scale decomposition in many previous studies (e.g. Moeng and Wyngaard 1988; Wyngaard et al. 1998; Kimmel et al. 2002; Kang 2009). Particularly in our study, given the sinusoidal shape of the surface heat-flux variation and the periodic lateral boundary conditions of large-eddy simulation, the Fourier spectral wave cut-off filter is an appropriate tool to analyze multi-scale features of u at 100 m above ground.

To apply the filter, the u field is first decomposed into Fourier modes,

$$u(x) = \sum_{\kappa_1} \hat{u}_{\kappa_1} e^{i\kappa_1 x}, \tag{3}$$

and the low-pass filter passes Fourier components of wavenumbers smaller than the cut-off wavenumber K and rejects those of wavenumbers larger than K . Thus the low-pass filtered² horizontal wind is

$$u_K^<(x) = \sum_{\kappa_1 < K} \hat{u}_{\kappa_1} e^{i\kappa_1 x}. \quad (4)$$

The complementary high-pass filter passes Fourier components of wavenumbers larger than K and rejects those smaller than K , i.e.,

$$u_K^>(x) = \sum_{\kappa_1 \geq K} \hat{u}_{\kappa_1} e^{i\kappa_1 x}, \quad (5)$$

The band-pass filter passes wavenumbers within a certain range of $K' \leq \kappa_1 \leq K$, and rejects wavenumbers outside that range:

$$u_{KK'}^<>(x) = (u_{K'}^>(x))^<_K = \sum_{\kappa_1 \geq K'}^{\kappa_1 < K} \hat{u}_{\kappa_1} e^{i\kappa_1 x}, \quad (6)$$

Figure 7 presents time evolutions of low-pass filtered u with $\lambda_1 > 32$ km, and band-pass filters of $8 \text{ km} < \lambda_1 \leq 32$ km, and $2 \text{ km} < \lambda_1 \leq 8$ km (where λ_1 is wavelength and $\lambda_1 = 2\pi/\kappa_1$) for cases A200A200L032 and A200L032, which are averaged along the y direction. In other words, for example, Fig. 7a shows u fluctuations that have wavelengths larger than 32 km, and Fig. 7b presents u fluctuations with wavelengths larger than 8 km and smaller than or equal to 32 km. Figure 7 demonstrates that, as scale decreases, the energy cascade becomes more discontinuous in space. On scales larger than 32 km, the convergence and divergence pattern is space-filling (Fig. 7a, b), but for smaller eddy scales the convergence and divergence patterns are discontinuous and less space filling (Fig. 7c–f). In the original Kolmogorov theory (Kolmogorov 1941), the energy cascade from the scale at which energy is introduced to the scale at which energy is dissipated is continuous and space filling at each step. However, many investigators including Kolmogorov himself later acknowledged that, as the energy cascade continues, the eddies become less and less space filling, with strong spatial gradients developing in conjunction with intermittent discontinuities, and thus the distribution becomes flatter than a Gaussian distribution (Frisch 1995; Davidson 2004).

The energy cascade that becomes less space filling on a scale smaller than 32 km is associated with interaction between eddies associated with the 128- and the 32-km surface heterogeneities. For example, large-scale circulations induced by the 128-km surface heterogeneity may produce subsidence and a strong capping inversion over that part of the surface that has heat fluxes smaller than the domain average, which is between $x = 0$ and 64 km. The subsidence reduces the intensity of small-scale circulations induced by the 32-km surface variation over the low surface heat-flux area. In order to further study the non-linear interaction between atmospheric fluctuations caused by large-scale and small-scale surface variations, the contributions of different scale fluctuations to $\langle u^2 \rangle^{1/2}$ are investigated for the two single-scale cases of A200L128 and A200L032 as well as for the multi-scale case of A200A200L032. The surface heterogeneity of A200A200L032 is composed of the two surface heterogeneities of A200A128 and A200L032 (Fig. 1).

² In this study, we follow the notation used in Frisch (1995) for the low-pass, high-pass, and band-pass filtered horizontal winds.

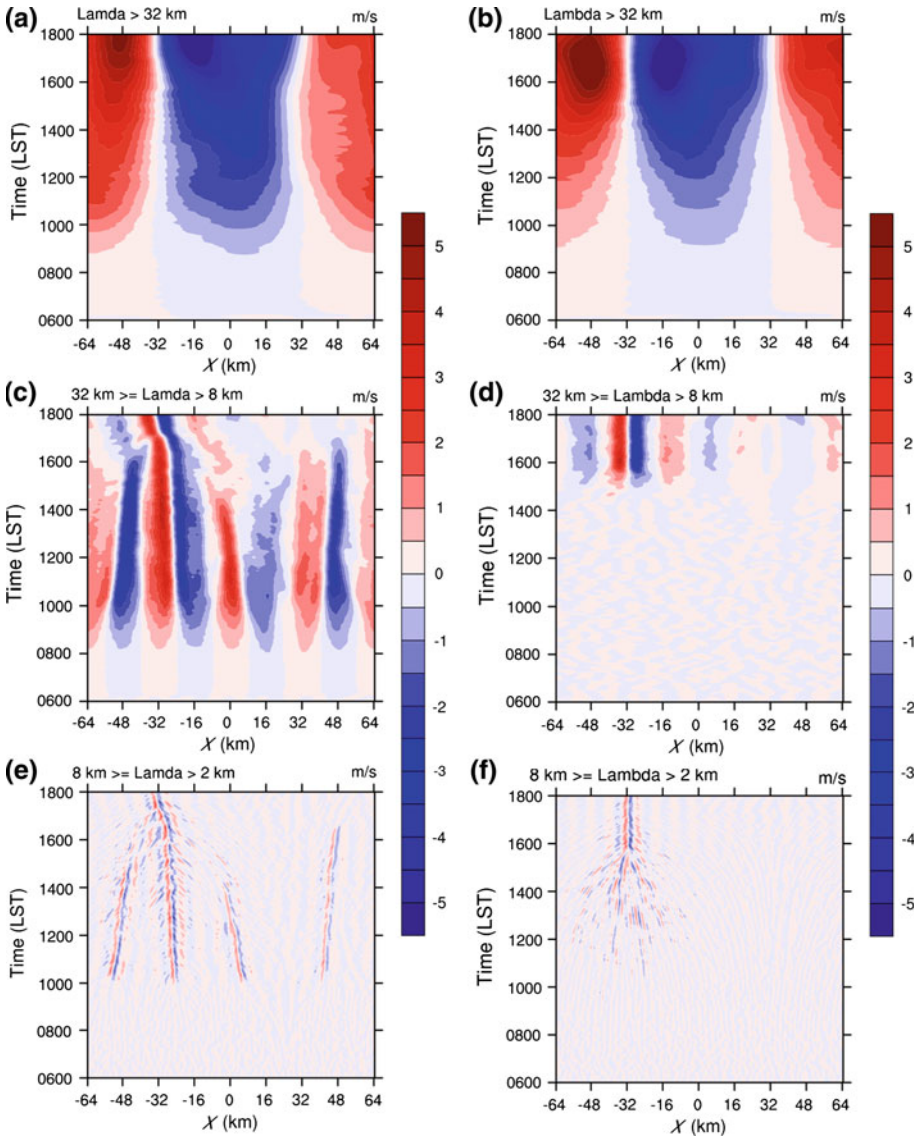


Fig. 7 Time evolution of u filtered with the low-pass of **a** $\lambda > 32$ km, and the band-pass of **c** $8 \text{ km} < \lambda \leq 32$ km, and **e** $2 \text{ km} < \lambda \leq 8$ km for case A200A200L032. Time evolution of u filtered with the low-pass of **b** $\lambda > 32$ km, and the band-pass of **d** $8 \text{ km} < \lambda \leq 32$ km, and **f** $2 \text{ km} < \lambda \leq 8$ km for case A200L128. The filtered u fields are averaged along the y direction. The unit of the colour scales is m s^{-1}

The characteristic velocity scale of $\langle u^2 \rangle^{1/2}$ is equivalent to the standard deviation of u , because $\langle u \rangle \approx 0$ in this study. That is,

$$\langle u^2 \rangle^{1/2} \approx \int_{-\infty}^{\infty} F_u(\kappa_1) d\kappa_1. \tag{7}$$

Herein, in order to measure the relative contribution of wind-speed fluctuations at each scale, to total fluctuations on all the scales, we define a ratio of spectral density in each wavenumber band to total power spectral density, viz.

$$R_n(t) \equiv \frac{\int_{|K_n|}^{|K_{n+1}|} F_u(\kappa_1) d\kappa_1}{\int_{-\infty}^{\infty} F_u(\kappa_1) d\kappa_1}, \quad (8)$$

where $K_n = 2\pi/L_n$ and $L_n = 2^{-n}\lambda_F$. Here, λ_F is the largest surface-heterogeneity wavelength for each case and $n = 0, 1, 2, \dots, N (= \log_2 \lambda_F)$. In other words, the smallest cut-off wavenumber K_0 is a function of the largest surface forcing scale. For example, $K_0 = 2\pi (128 \text{ km})^{-1}$ for case A200A200L032 but $K_0 = 2\pi (32 \text{ km})^{-1}$ for case A200L032 because the largest forcing scale is 128 km for A200A200L032, but 32 km for A200L032. Then $K_1 = 2\pi (64 \text{ km})^{-1}$ for A200A200L032 but $K_1 = 2\pi (16 \text{ km})^{-1}$ for A200L032.

Figure 8 presents the time evolution of the relative variance contribution ratios for the two single-scale cases A200L128 and A200L032, and for the multi-scale case A200A200L032. For the two single-scale cases (Fig. 8a, b), the variance contribution (R_0) from the fluctuations on the scale of the surface heterogeneity itself steadily grows until reaching the oscillation onset of wind speed, and then becomes dominant. Around the peak of the temporal fluctuation, the contribution (R_1) from the fluctuations over the wavelength interval $L_1 (= 2^{-1}\lambda_F) \leq \lambda < L_0 (= \lambda_F)$ significantly increases. The increased R_1 implies that spectral energy cascades down to wavelengths smaller than the heterogeneity scale itself. The downscale energy cascade extends down to a certain smaller wavelength, as shown with the increased R_2 and R_3 around the oscillation onset. As scale decreases further down to the turbulence scale, however, time evolution of R_n becomes negatively correlated to that of R_0 ; that is, increased mesoscale wind-speed fluctuations reduce wind fluctuations on the turbulence scale.

In order to identify at which scale the correlation relationship between R_0 and R_n undergoes transition from positive to negative, we compute the correlation coefficients between the temporal evolution of R_0 and R_n , $\rho(R_0, R_n)$, which is shown in Table 2. For a scale smaller than 2 km, R_n is highly negatively correlated with R_0 . Turbulence is controlled through stability modified by the surface-heterogeneity-induced mesoscale flows. Kang and Davis (2008), who used a similar numerical set-up, found that cold air advection in the lower ABL and warm advection in the upper ABL that are associated with induced mesoscale flows create a slight stable stratification from the domain-averaged perspective. The effective resolution of the Bryan and Fritsch (2002) model is 6Δ , where Δ is the grid spacing (Bryan et al. 2003). The horizontal grid spacing is 100 m, and on a scale smaller than the effective resolution of 600 m the negative correlation coefficient between temporal evolutions of R_0 and R_n , $\rho(R_0, R_n)$, may be associated with numerical dissipation. However, negative $\rho(R_0, R_n)$ on a scale somewhat larger than the effective resolution of 600 m is associated with turbulence reduction, due to increased stability, by induced mesoscale flows.

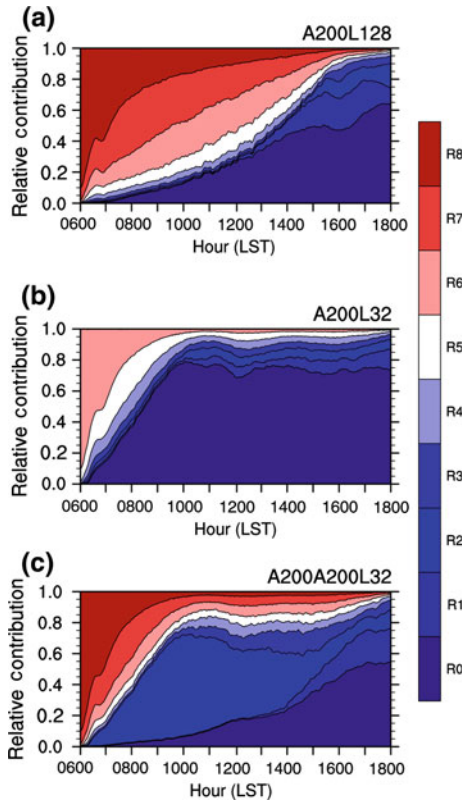
In Fig. 8c, the multi-scale case of A200A200L032 has two forcing scales: $L_0 (= 128 \text{ km})$ and $L_2 (= 32 \text{ km})$. Before 1200 LST, the contribution to variance from the scale L_2 is dominant. However, after 1200 LST, the contribution of the scale L_0 rapidly increases and becomes dominant. Furthermore, the temporal evolution of the ratio R_2 that is associated with the second forcing scale $L_2 (= 32 \text{ km})$ is poorly correlated with that of the ratio R_3 that is associated with the scale one wavelength smaller than the forcing scale (16 km). The correlation coefficient $\rho(R_0, R_1)$ is significantly positive for all the multi-scale cases, which is also true for all the single-scale cases (Tables 2, 3). Unlike $\rho(R_0, R_1)$, the correlation

Table 2 Correlation coefficients between R_0 and R_T for the single-scale cases

Case	$\rho(R_0, R_T)$, where the R_T is associated with the spectral density in the scale range of									
	$\lambda \geq 128$	$128 > \lambda \geq 64$	$64 > \lambda \geq 32$	$32 > \lambda \geq 16$	$16 > \lambda \geq 8$	$8 > \lambda \geq 4$	$4 > \lambda \geq 2$	$2 > \lambda \geq 1$	$\lambda < 1$	
A200L128	1	0.85	0.75	0.69	0.04	-0.34	-0.57	-0.87	-0.80	
A050L128	1	0.97	0.41	0.76	0.68	0.56	0	-0.67	-0.49	
A200L032			1	0.59	0.72	-0.18	-0.63	-0.83	-0.95	
A050L032			1	0.90	0.86	-0.02	-0.51	-0.86	-0.82	
A200L016				1	0.57	0.75	-0.43	-0.80	-0.97	
A050L016				1	0.92	0.79	-0.13	-0.80	-0.89	

The ratios, R_T is defined in Sect. 3.3

Fig. 8 Time evolutions of the relative contributions of the components of (8) to $\langle u^2 \rangle^{1/2}$ for cases **a** A200L128, **b** A200L032, and **c** A200A200L032. As shown in the colour bar on the right, each colour represents the relative variance contribution ratio of R_n ($n = 0, 1, 2, 3, \dots, \log_2 \lambda_F + 1$, where λ_F is the surface forcing scale), which is defined in Sect. 3.3



coefficient between the temporal evolution of the ratio R_2 (or R_3) at the second forcing scale of 32 km (or 16 km), and the ratio R_3 (or R_4) at the scale one wavelength smaller than the second forcing scale is insignificant, as shown in Table 4. The poor correlations are associated with non-linear interactions between the eddies on the first and second forcing scales. In other words, the multi-scale forcing case creates a different environment for the atmospheric flows generated by the small-scale forcing, which needs to be further explored in detail in future work with more realistic surface and atmospheric conditions for practical applications of these results.

For the multi-scale surface heterogeneity, when the large-scale surface heterogeneity is strong (e.g., A200A200L032), turbulence is primarily controlled by atmospheric fluctuations associated with the large-scale surface forcing. In contrast, when the large-scale surface heterogeneity is weak (e.g., A050A200L032), turbulence is controlled by atmospheric fluctuations that are associated with small-scale surface forcing.

In Tables 3 and 4, when the amplitude of the 128-km surface heat-flux variation is 200 W m^{-2} , the ratios that are associated with 2 km or smaller scales (R_7 and R_8) have significant negative correlations with R_0 , the ratio associated with 128 km. However, when the amplitude of the 128-km surface heat-flux variation is 50 W m^{-2} , R_7 and R_8 have significant negative correlations with R_2 (or R_3), the ratio associated with the second forcing scale of 32 km (or 16 km).

Table 3 Correlation coefficients between R_0 and R_n for the single-scale cases

Case	$\rho(R_0, R_n)$, where the R_n is associated with the spectral density in the scale range of								
	128	64	32	16	8	4	2	1	<1
A200A200L032	1	0.95	-0.52	0.47	0.26	-0.41	-0.74	-0.70	-0.51
A200A200L016	1	0.94	0.86	-0.70	0.06	-0.44	-0.71	-0.67	-0.43
A200A050L032	1	0.89	0.12	0.60	0.33	-0.44	-0.70	-0.89	-0.76
A200A050L016	1	0.89	0.84	-0.39	0.08	-0.45	-0.73	-0.90	-0.71
A050A200L032	1	0.85	0.15	0.85	0.78	-0.14	-0.47	-0.44	-0.32
A050A200L016	1	0.97	0.71	-0.32	0.91	0.60	-0.07	-0.26	-0.21
A050A050L032	1	0.83	0.50	0.97	0.71	-0.24	-0.62	-0.66	-0.46
A050A050L016	1	0.96	0.61	-0.05	0.87	0.43	-0.36	-0.52	-0.35

The ratios, R_0 and R_n are defined in Sect. 3.3

Table 4 Correlation coefficients between R_2 and R_n for the surface heterogeneity that includes the 32-km surface forcing, and between R_3 and R_n for the heterogeneity that includes the 16-km surface forcing

Case	$\rho(R_{2\text{or}3}, R_n)$, where the R_n is associated with the spectral density in the scale range of								
	$\lambda \geq 128$	$126 > \lambda \geq 64$	32	16	8	4	2	1	<1
A200A200L032	-0.52	-0.63	1.00	0.02	0.28	0.36	0.28	-0.05	-0.40
A200A200L016	-0.70	-0.74	-0.63	1.00	0.09	0.57	0.44	0.10	-0.28
A200A050L032	0.12	-0.03	1.00	0.12	0.14	-0.32	-0.35	-0.09	-0.54
A200A050L016	-0.39	-0.53	-0.45	1.00	0.32	0.67	0.74	0.38	-0.26
A050A200L032	0.15	-0.09	1.00	0.44	0.53	-0.12	-0.55	-0.78	-0.93
A050A200L016	-0.32	-0.36	-0.24	1.00	-0.04	0.25	-0.33	-0.64	-0.83
A050A050L032	0.50	0.25	1.00	0.63	0.85	0.39	-0.33	-0.80	-0.84
A050A050L016	-0.05	-0.14	0.26	1.00	0.29	0.69	0.31	-0.55	-0.82

The ratio R_n is defined in Sect. 3.3

3.4 Distribution of Velocity Increments

In order to investigate the velocities of turbulent eddies on a scale l over the single- and multi-scale surface heterogeneity, we use velocity increments over a distance l :

$$\delta u_l = u(x + l) - u(x), \tag{9}$$

where the distance l is chosen to be 1 km, which is close to the scale at which the turbulent spectral density peaks in the spectra shown in Figs. 4, 5, and 6. Based on Bryan et al. (2003), given $\Delta x = 100$ m, the effective resolution is about 600 m, so that 1-km eddies are explicitly resolved here. Figure 9 presents the probability density functions (PDF) of $\delta u_l/\sigma$, $p(\delta u_l/\sigma)$, at 0800, 1100, 1700 LST, where σ is the standard deviation of the velocity increment at each time. As shown in Fig. 9, $p(\delta u_l/\sigma)$ for the horizontally homogeneous CBL (A000L000) is approximately Gaussian at each time. However, for case A200A200L032 the PDF at 0800 LST remains Gaussian, but the PDFs at 1100 and 1700 LST are strongly non-Gaussian, and have exponential tails resulting in negative skewness and large kurtosis.

The 1-km eddies are not in the turbulence inertial range between the integral scale (the scale that characterizes the energy-containing eddies; Lenschow and Stankov 1986) and the Kolmogorov scale (the scale that characterizes the onset of the dissipation-scale eddies).

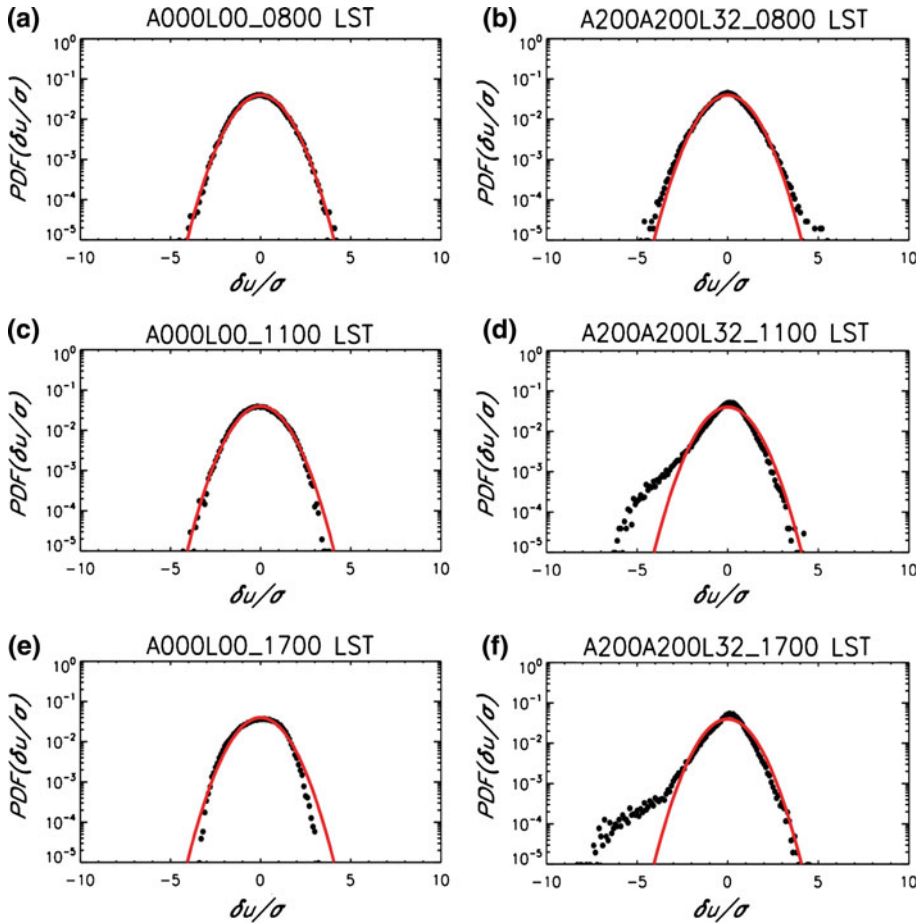


Fig. 9 Probability density function (PDF) of the velocity increment (δu_l) that is normalized with the standard deviation of u at each time (σ). The distance l for the velocity increment is chosen to be 1 km. The normalized PDFs are obtained at 0800 LST (**a** and **b**), 1100 LST (**c** and **d**), and 1700 LST (**e** and **f**) for cases A000L000 (**a**, **c**, and **e**) and A200A200L032 (**b**, **d**, and **f**). The *solid lines* come from the Gaussian distribution assumption and the *symbols* come from LES results

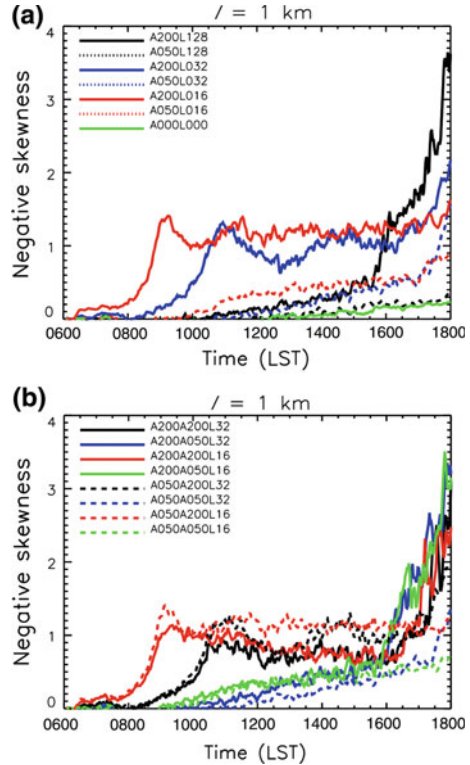
However, these eddies are much smaller than the surface forcing scales, and transfer of energy from the forcing scales to smaller scales lying between the integral and dissipation scales is to be expected. For the choice for l , and scale of surface heterogeneity, it is unlikely that 1-km eddies are homogeneous and isotropic. However, the negative skewness is analogous to the well-known negative skewness of homogeneous and isotropic turbulence in the inertial range.

In the simplest case, Kolmogorov's four-fifths law (Kolmogorov 1941) states that, for homogeneous and isotropic turbulence in the inertial range,

$$\langle \delta u_l^3 \rangle = -(4/5)\varepsilon l, \quad (10)$$

where ε is the eddy dissipation, equal to the flux of energy across the scale l (Frisch 1995; Davidson 2004). Thus, the negative skewness of the velocity increment ($\langle \delta u_l^3 \rangle / \langle \delta u_l^2 \rangle^{3/2} < 0$)

Fig. 10 **a** Time evolutions of normalized velocity increment ($\delta u_1/\sigma$) skewness for the single-scale cases. Here the separation distance l is 1 km. **b** Same as **(a)** except for the multi-scale cases



indicates a positive transfer of energy to smaller scales ($\varepsilon > 0$). Kolmogorov’s four-fifths law derives from the Karman–Howarth theorem for isotropic and homogeneous turbulence, which gives an exact relation between third-order moments of the velocity, forcing, dissipation, and energy flux across scales. It was generalized to the Navier–Stokes equation in homogeneous but anisotropic cases by Monin and Yaglom (1975), and also to inhomogeneous flows as, for example, in the presence of stratification. In this context it is important to note that negative skewness associated with an energy flux to smaller scales (e.g., because of vortex stretching) in a scale range of cascade processes (e.g., Lindborg 1999; Gotoh 2001; Vindel et al. 2008) results from these exact laws, and is independent of Kolmogorov’s original assumption of self-similarity that does not apply to intermittent turbulence (Frisch 1995; Davidson 2004) as studied here.

In order to quantify negative skewness increases at the temporal fluctuation onsets, we plot the time evolution of the skewness of the normalized velocity increment in Fig. 10a for the single-scale cases and in Fig. 10b for the multi-scale cases. In Fig. 10a, for the low-amplitude surface variation cases in which oscillations of wind speed are absent, the negative skewness steadily grows with time. However, for the high-amplitude surface variation cases, the negative skewness suddenly increases at the oscillation onset. This result is consistent with the suggestion of Kang (2009) that at the peak of the temporal fluctuation, energy cascades occur, which we previously confirmed with the spectral analysis shown in Figs. 4, 5, and 6. For the multi-scale cases with high-amplitude surface heterogeneities both on large and small scales (A200A200L32 and A200A200L16 in Fig. 10b), multiple sudden increases of the negative skewness occur.

Compared with the multi-scale surface heterogeneity cases with low-amplitude surface heterogeneity on a large scale (A050A200L32: dotted black line, and A050A200L16: dotted red line in Fig. 10b), the cases with high-amplitude surface heterogeneity on a small scale (A200A200L32: solid black line, and A200A200L16: solid red line in Fig. 10b) show smaller negative skewness between the first peak of the temporal fluctuation (0900 LST or 1100 LST) and 1600 LST. The smaller negative skewness is likely associated with a weaker energy cascade. When mesoscale flows are generated by high-amplitude surface heterogeneity, turbulence is reduced due to significant modulation of stability by lower-level cold advection and upper-level warm advection (Kang and Davis 2008), which we confirmed with the correlation coefficients presented in Tables 2, 3, and 4. Thus, after the first oscillation onset, the horizontal flows generated by high-amplitude surface heterogeneity on a large scale control overall stability and more strongly reduce turbulence compared with the cases with low-amplitude surface heterogeneity on a large scale.

Near the energy injection scale, a Gaussian PDF of the normalized velocity increment is often observed. Although such PDFs can be explained by the original Kolmogorov theory (Kolmogorov 1941), later studies suggested that, as the energy cascade continues, eddies become decreasingly space filling (Frisch 1995; Davidson 2004). In other words, for a separation distance close to the energy injection scale, the PDF of the normalized velocity increment approaches a Gaussian. But, as the eddy scale diminishes, the PDFs generate stretched exponential tails (i.e. a larger kurtosis) as a result of an intermittent energy cascade (Frisch 1995; Davidson 2004), which is characterized by the appearance of many sharp peaks in the space or time series. Also, the intermittent cascade model associated with a large kurtosis of the velocity-increment PDF has been applied to eddy scales in the ABL much larger than the integral scale of the turbulence (e.g., Lauren et al. 2001; Davidson 2004; Muzy et al. 2010).

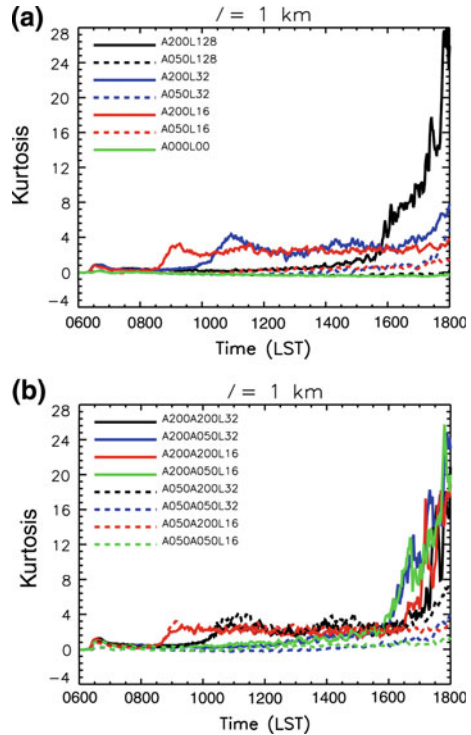
We also plot the time evolution of the kurtosis³ of the velocity increment PDF in Fig. 11a for the single-scale cases and in Fig. 11b for the multi-scale cases. Given that the kurtosis of the velocity increment PDF is associated with intermittency of the turbulence, the increase of the kurtosis at the fluctuation onsets can be interpreted as an increase in intermittency. Figure 11a shows that, at the fluctuation onsets for the single-scale cases, the kurtosis suddenly increases. In particular, for the cases with high-amplitude surface variation on the large scale of 128 km (solid black line in Fig. 11a), the intermittency increase is very sudden. This sudden rise is also obvious in the multi-scale cases with the high-amplitude surface variation on the large scale (solid lines in Fig. 11b). This result implies that a horizontal wind that initially has a Gaussian distribution characteristic of flow over a horizontally homogeneous surface can suddenly change into a gusty wind that has large intermittency in the late afternoon due to the effect of surface heterogeneity at a hundred kilometre scale.

4 Summary and Conclusions

We investigate horizontal wind speeds induced by mesoscale surface heterogeneity at 100 m above ground, a typical wind-turbine hub height, under zero background flow, by using LES with a grid spacing of 100 m over a horizontal domain of 128 km \times 8 km. Mesoscale surface heterogeneity is prescribed with sinusoidal surface heat-flux variations that have wavelengths of 16, 32, or 128 km and amplitudes of 50 or 200 W m⁻² over the daytime diurnal cycle between 0600 and 1800 LST. Thus, the sinusoidal surface heat-flux variations

³ In this study, kurtosis is defined as the fourth moment around the mean (μ_4) divided by the square of the variance (σ^4) of the probability distribution minus 3, namely $\mu_4/\sigma^4 - 3$.

Fig. 11 **a** Time evolutions of the normalized velocity increment ($\delta u_l/\sigma$) kurtosis for the single-scale cases. Here the separation distance l is 1 km. **b** Same as **(a)** except for the multi-scale cases



have maximum amplitudes of 50 or 200 W m⁻² at midday, and minimum amplitudes of zero at 0600 and 1800 LST. The results demonstrate that only for surface variations that have maximum amplitudes of 200W m⁻², the induced horizontal wind speeds temporally fluctuate within the daytime diurnal cycle.

We investigate the temporal oscillation characteristics of wind speed. For low-level horizontal wind speeds induced by the surface variations on scales of 16 and 32 km, oscillation onsets occur first before noon. The amplitudes of the oscillations associated with the surface variations on scales of 16 and 32 km are small compared with the amplitudes associated with the surface variation on a scale of 128 km. For the single-scale case with a surface variation scale of 128 km, the oscillation onset occurs once in the late afternoon (about 1700 LST). However, for the multi-scale cases in which a 16- or 32-km surface heat-flux variation is superimposed on the 128-km surface variation, multiple oscillation onsets occur: one associated with the 10-km order surface variation has its peak before noon and the other one associated with the 128-km variation has its peak in the late afternoon.

We also investigate intermittent discontinuities of 1-km scale eddies in space, which is associated with the wind-speed oscillations. When oscillations occur, the energy at the given surface heterogeneity scale cascades down to smaller-scale eddies. Fourier spectral decomposition demonstrates that, as the energy cascade progresses, eddies are increasingly discontinuous in space with decreasing eddy scales. In order to investigate the increase of spatial intermittency, we use the kurtosis of the velocity increment with a separation distance of 1 km. For all cases with an oscillatory wind speed, the spatial discontinuity of 1-km scale eddies rapidly and significantly increases at the oscillation onsets. In other words, with an oscillatory winds the 1-km scale eddies are not homogeneously distributed, but instead

become heterogeneously distributed with high spatial variability. In particular, at the oscillation onset of the 128-km surface heterogeneity case, the kurtosis of the velocity increment increases the most among all the cases.

In the CBL incorporating the horizontal flows induced by mesoscale surface heterogeneity, the discontinuous increase of 1-km scale eddies is associated with the increase of static stability over the whole domain. The static stability increase is the result of cold advection in the lower part of the CBL and warm advection in the upper part due to the induced horizontal flows (Kang and Davis 2008). In other words, the overall static stability that is associated with the induced horizontal flows controls the eddies on scales comparable to, or smaller than, the CBL height. We show that the correlation coefficients between the temporal evolution of the band-pass filtered relative variances R_0 and R_n , $\rho(R_0, R_n)$, undergo transition from positive to negative values at about 2-km wavelength. For the cases with the multi-scale surface variation that are comprised of the two single-scale variations on scales of 128 km and either 16 or 32 km, 2-km or smaller-scale eddies are primarily controlled by the horizontal flows associated with the higher-amplitude surface variation. When the two variation amplitudes are the same, the small-scale eddies are mostly controlled by the horizontal flows induced by the larger-wavelength surface variation.

The impact of local surface heterogeneity on the atmospheric flow could be more substantial under weak synoptic flow. Given that an NWP system for wind power forecasting is usually a mesoscale model that has a limitation in precisely representing local surface heterogeneity, wind-speed oscillations could be poorly predicted. In the absence of significant synoptic forcing, wind-speed oscillations may result in unanticipated rapid jumps in wind-power output. Thus, we suggest that the temporally oscillating wind speeds that are induced by local surface heterogeneity could be one of the fundamental reasons for unpredicted rapid jumps in wind-power production.

Even with precise information on local surface heterogeneity, an NWP system may still have limitations in exactly predicting wind-speed oscillations. Usually a mesoscale model employs a one-dimensional ABL ensemble-mean model parametrization that assumes homogeneity. With a horizontal grid spacing that is usually larger than the typical CBL height of 1 km, each atmospheric parameter is represented with a constant value. In addition, the atmospheric fluctuations on scales smaller than the effective resolution, which is usually 4–7 times the actual grid spacing, are reduced by numerical dissipation. Thus in a mesoscale model, turbulent ABL flows may be distorted particularly on scales smaller than the effective resolution. In other words, these oscillatory events, which result in significant sudden spatial discontinuities in the wind on scales close to the ABL height or smaller may not be correctly predicted by a mesoscale model.

In future studies, we plan to test the dependence of mesoscale model results on the model resolution by comparing with LES results from the aspect of oscillatory events and their associated energy cascade processes. Studying the performance of ABL parametrization schemes in higher resolution mesoscale models is an active and important research field (e.g., Martínez et al. 2010; Honnert et al. 2011). Using both a high-resolution mesoscale model and a LES code, we plan to also test the hypothesis that temporal oscillations and their associated increases in spatial discontinuity of eddies on scales of a few kilometres or smaller can result in localized abrupt changes in horizontal wind speeds under various background wind conditions.

Acknowledgments We would like to acknowledge high-performance computing support provided by NCAR's Computational and Information System Laboratory, sponsored by the National Science Foundation. The authors also thank Drs. Margaret LeMone, George Bryan, and Pablo Mininni for providing reviews

of an earlier version of this manuscript. Helpful comments provided by two anonymous reviewers are also greatly appreciated.

References

- Anthes RA (1984) Enhancement of convective precipitation by mesoscale variations in vegetative covering in semiarid regions. *J Appl Meteorol* 23:541–554
- Avissar R, Schmidt T (1998) An evaluation of the scale at which ground-surface heat flux patchiness affects the convective boundary layer using large-eddy simulations. *J Atmos Sci* 55:2666–2688
- Baldi M, Dalu GA, Pielke RA (2008) Vertical velocities and available potential energy generated by landscape variability-theory. *J Appl Meteorol* 47:397–410
- Böttcher F, Renner C, Waldl HP, Peinke J (2003) On the statistics of wind gusts. *Boundary-Layer Meteorol* 108:163–173
- Böttcher F, Barth St, Penike J (2007) Small and large scale fluctuations in atmospheric wind speeds. *Stoch Env Res Risk Assess* 21:299–308
- Bryan GH, Fritsch JM (2002) A benchmark simulation for moist nonhydrostatic numerical models. *Mon Weather Rev* 130:2917–2928
- Bryan GH, Wyngaard JC, Fritsch JM (2003) Resolution requirements for the simulation of deep moist convection. *Mon Weather Rev* 131:2394–2416
- Chen F, Avissar F (1994) The impact of land-surface wetness heterogeneity on mesoscale heat fluxes. *J Appl Meteorol* 33:1323–1340
- Courault D, Seguin B, Olioso A (2005) Review about estimation of evapotranspiration from remote sensing data: from empirical to numerical modeling approach. *Irrig Drain Syst* 19:223–249
- Dalu GA, Pielke RA (1993) Vertical heat fluxes generated by mesoscale atmospheric flow induced by thermal inhomogeneities in the PBL. *J Atmos Sci* 50:919–926
- Davidson PA (2004) *Turbulence: an introduction for scientists and engineers*. Oxford University Press, Oxford, 653 pp
- Davis JC, Collier CG, Davies F, Bozier KE (2008) Spatial variations of sensible heat flux over an urban area measured using Doppler lidar. *Meteorol Appl* 15:367–380
- Deardorff JW (1980) Stratocumulus-capped mixed layers derived from a three-dimensional model. *Boundary-Layer Meteorol* 18:495–527
- Durrant DR, Klemp JB (1983) A compressible model for the simulation of moist mountain waves. *Mon Weather Rev* 111:2341–2361
- Esau IN (2007) Amplification of turbulent exchange over wide arctic leads: large-eddy simulation study. *J Geophys Res* 112:D08109. doi:[10.1029/2006JD007225](https://doi.org/10.1029/2006JD007225)
- Fedorovich E, Conzemius R, Esau F, Chow K, Lewellen D, Moeng C-H, Pino D, Sullivan P, Vilá-Guerau de Arellano J (2004) Entrainment into sheared convective boundary layers as predicted by different large eddy simulation codes. Preprints. In: 16th Symposium on boundary layers and turbulence, American Meteorological Society, 9–13 August, Portland, Maine, USA, CD-ROM, P4.7
- Findell KL, Eltahir AB (2003) Atmospheric controls on soil moisture–boundary layer interactions. Part I: Framework development. *J Hydrometeorol* 4:552–569
- Frisch U (1995) *Turbulence: the legacy of A.N. Kolmogorov*. Cambridge University Press, Cambridge, 296 pp
- Giebel G (2003) The state-of-the-art in short-term prediction of wind power: a literature overview. Project Anemos, Riso National Laboratory Tech. Rep., Roskilde, Denmark, 36 pp
- Gotoh T (2001) Turbulence research at large Reynolds numbers using high resolution DNS. *RIKEN Rev* 40:3–6
- Hidalgo J, Pigeon G, Masson V (2008) Urban-breeze circulation during the CAPITOUL experiment: observational data analysis approach. *Meteorol Atmos Phys* 102:223–241
- Hidalgo J, Masson V, Gimeno L (2010) Scaling the daytime urban heat island and urban-breeze circulation. *J Appl Meteorol* 49:889–901
- Holt TR, Niyogi D, Chen F, Manning K, LeMone MA, Qureshi A (2006) Effect of land–atmosphere interactions on the IHOP 24–25 May 2002 convection case. *Mon Weather Rev* 134:113–133
- Honnert R, Masson V, Couvreur F (2011) A diagnostic for evaluating the representation of turbulence in atmospheric models at the kilometeric scale. *J Atmos Sci*. doi:[10.1175/JAS-D-11-061.1](https://doi.org/10.1175/JAS-D-11-061.1)
- Inoue J, Kawashima M, Fujiyoshi Y, Wakatsuchi M (2005) Aircraft observations of air-mass modification over the sea of Okhotsk during sea-ice growth. *Boundary-Layer Meteorol* 117:111–129

- Kang S-L (2009) Temporal oscillations in the convective boundary layer forced by mesoscale surface heat-flux variations. *Boundary-Layer Meteorol* 132:59–81
- Kang S-L, Bryan GH (2011) A large eddy simulation study on moist convection initiation over heterogeneous surface fluxes. *Mon Weather Rev* 139:2901–2917
- Kang S-L, Davis KJ (2008) The effects of mesoscale surface heterogeneity on the fair-weather convective atmospheric boundary layer. *J Atmos Sci* 65:3197–3213
- Kang S-L, Davis KJ, LeMone M (2007) Observations of the ABL structures over a heterogeneous land surface during IHOP_2002. *J Hydrometeorol* 8:221–244
- Kimmel SJ, Wyngaard JC, Otte MJ (2002) “Log-Chipper” turbulence in the convective boundary layer. *J Atmos Sci* 59:1124–1134
- Kolmogorov AN (1941) Energy dissipation in locally isotropic turbulence. *Dokl Akad Nauk SSSR* 32:19–21
- Lauren MK, Menabde M, Seed AW, Austin GL (1999) Characterization and simulation of the multiscaling properties of the energy-containing scales of horizontal surface-layer winds. *Boundary-Layer Meteorol* 90:21–46
- Lauren MK, Menabde M, Austin GL (2001) Analysis and simulation of surface-layer winds using multiplicative cascade models with self-similar probability densities. *Boundary-Layer Meteorol* 100:263–286
- Lenschow DH, Stankov BB (1986) Length scales in the convective boundary layer. *J Atmos Sci* 43:1198–1209
- Letzel MO, Raasch S (2003) Large eddy simulation of thermally induced oscillations in the convective boundary layer. *J Atmos Sci* 60:2328–2340
- Lindborg E (1999) Can the atmospheric kinetic energy spectrum be explained by two-dimensional turbulence? *J Fluid Mech* 388:259–288
- Liu G, Sun J, Yin L (2011) Turbulence characteristics of the shear-free convective boundary layer driven by heterogeneous surface heating. *Boundary-Layer Meteorol* 140:57–71
- Mahrt L, Sun J, Vickers D, MacPherson JI, Pederson JR, Desjardins RL (1994) Observations of fluxes and inland breezes over a heterogeneous surface. *J Atmos Sci* 51:2484–2499
- Martínez D, Jiménez MA, Cuxart J, Mahrt L (2010) Heterogeneous nocturnal cooling in a large basin under very stable conditions. *Boundary-Layer Meteorol* 137:97–113
- Moeng C-H, Wyngaard JC (1988) Spectra analysis of large-eddy simulations of the convective boundary layer. *J Atmos Sci* 45:3573–3587
- Monin AS, Yaglom AM (1975). *Statistical fluid mechanics*. MIT Press, Cambridge, 874 pp
- Muzy J-F, Baile R, Poggi P (2010) Intermittency of surface-layer wind velocity series in the mesoscale range. *Phys Rev E* 81:056308. doi:10.1103/PhysRevE.81.056308
- Raasch S, Harbusch G (2001) An analysis of secondary circulations and their effects caused by small-scale inhomogeneities using large-eddy simulation. *Boundary-Layer Meteorol* 101:31–59
- Rohrig K, Lange B (2007) Improvement of the power system reliability by prediction of wind power generation. In: *Power Engineering Society general meeting*, IEEE, 24–28 June 2007, pp 1–8
- Rotunno R (1983) On the linear theory of the land and sea breeze. *J Atmos Sci* 40:1999–2009
- Shen S, Leclerc MY (1995) How large must surface inhomogeneities be before they influence the convective boundary layer structure? A case study. *Q J R Meteorol Soc* 121:1209–1228
- Stull RB (1988) *An introduction to boundary layer meteorology*. Kluwer Academic Publisher, Dordrecht, 670 pp
- Vindel JM, Yague C, Redondo JM (2008) Structure function analysis and intermittency in the atmospheric boundary layer. *Nonlinear Proc Geophys* 15:915–929
- Wang W (2009) The influence of thermally-induced circulations on turbulence statistics over an idealized urban area under a zero background wind. *Boundary-Layer Meteorol* 131:403–423
- Wang J, Bars RL, Eltahir EA (1996) A stochastic linear theory of mesoscale circulation induced by the thermal heterogeneity of the land surface. *J Atmos Sci* 53:3349–3366
- Weaver CP, Avissar R (2001) Atmospheric disturbances caused by human modification of the landscape. *Bull Am Meteorol Soc* 82:269–281
- Weckwerth TM et al (2004) An overview of the International H2O Project (IHOP_2002) and some preliminary highlights. *Bull Am Meteorol Soc* 85:253–277
- Wicker LJ, Skamarock WC (2002) Time-splitting methods for elastic models using forward time schemes. *Mon Weather Rev* 130:2088–2097
- Wyngaard JC, Peltier LJ, Khanna S (1998) LES in the surface layer: surface fluxes, scaling, and SGS modeling. *J Atmos Sci* 55:1733–1754
- Zhang CL, Chen F, Miao SG, Li QC, Xia XA, Xuan CY (2009) Impacts of urban expansion and future green planting on summer precipitation in the Beijing metropolitan area. *J Geophys Res* 114(D2):D02116